Analysis of ICRF Wave Heating in the Wendelstein VII-AS Stellarator

K. Itoh[1], S.I. Itoh[2], A. Fukuyama[3], J.-M. Noterdaeme[4], and H. Wobig[4]

IPP 2/289

September 87

MAX-PLANCK-INSTITUT FÜR PLASMAPHYSIK

8046 GARCHING BEI MÜNCHEN

MAX-PLANCK-INSTITUT FÜR PLASMAPHYSIK

GARCHING BEI MÜNCHEN

Analysis of ICRF Wave Heating in the Wendelstein VII-AS Stellarator

K. Itoh[1], S.I. Itoh[2], A. Fukuyama[3], J.-M. Noterdaeme[4], and H. Wobig[4]

IPP 2/289 September 87

1) Plasma Physics Laboratory, Kyoto University
2) Institute for Fusion Theory, Hiroshima University
3) School of Engineering, Okayama University
4) Max-Planck-Institute für Plasmaphysik

Die nachstehende Arbeit wurde im Rahmen des Vertrages zwischen dem Max-Planck-Institut für Plasmaphysik und der Europäischen Atomgemeinschaft über die Zusammenarbeit auf dem Gebiete der Plasmaphysik durchgeführt.

ABSTRACT

The propagation and absorption of the ICRF (ion cyclotron range of frequencies) waves in the Wendelstein VII-AS stellarator is studied. Both the cases of the two-ion hybrid resonance heating and second harmonic cyclotron resonance heating are investigated by solving the global wave equation. Accessibility range and antenna loading impedance for various plasma parameters as well as the power deposition profile are obtained. The generation of fast ions is also discussed.

1) INTRODUCTION

High power ICRF (ion cyclotron range of frequencies) heating has become a dependable method for the heating of toroidal plasmas[1-7]. Experimental and theoretical studies of tokamak plasmas have made progress, and the importance of the various physical processes, such as the wave propagation and absorption, thermalization of absorbed energy, generation of high energy particles, spatial transport and interactions with scrape-off layer (SoL) plasma, are more and more clearly understood[8-12]. In stellarators, the ICRF waves, which were first applied to the C-Stellarator[1], are successfully applied to the Heliotron E device[8], and are also planned[13] for the Wendelstein VII-AS modular stellarator[14] as well as for the ATF device[15]. The ICRF wave heating is usually associated with high energy ions[9], which shows a different spatial loss character affecting the ambipolarity of the particle flux. The important role of the radial electric field on the stellarator transport has been recognized[16-18]. Therefore the ICRF heating, which in principle can supply the energy without the additional particle supply, is of particular importance for the understanding of transport phenomena in stellarators.

In analyzing ICRF heating, the rf-wave is solved as a boundary value problem. This method is relevant because the wave length is comparable to the plasma geometry (minor radius in small machines, antenna-plasma distance in larger machines) and a complicated propagation structure (resonance-cut off surfaces) exists in the plasma. By this method, the power deposition profile and the antenna loading impedance can be calculated in tokamaks[11,12,19] and torsatron/stellarators[20].

In this article we solve the ICRF wave equation in a model geometry of the W VII-AS modular stellarator for the cases of the two-ion hybrid resonance heating and the second cyclotron resonance heating. The accessibility of the fast wave, power deposition profile and power partition are obtained. The antenna loading resistance is calculated. It is shown that the effect of the cavity resonance is important in the range of $n_e \lesssim 10^{20}/m^3$. The energy of the generated high energy particle is also discussed.

2) MODEL AND BASIC EQUATION

We choose a simplified model geometry of W VII-AS. Figure 1 illustrates the poloidal cross-section and the cross-section on the equatorial plane near the ICRF wave antenna. In the region in Fig. 1, the major component of the magnetic field variation comes from the toroidal effect. The elongation of the plasma is large and the vertical variation is weaker compared to the variation in the major radius direction. We therefore take a simplified model geometry shown in Fig. 2. We neglect the inhomogenity in the vertical and toroidal directions and solve the wave in a one-dimensional slab geometry. This assumption may be too crude, but we accept it as the first step of the analysis.

The model distributions of the magnetic field density and temperatures are chosen as

$$B(x) = \frac{B_o}{1 + x/R} \quad , \tag{1}$$

$$n_j(x) = (n_{oj} - n_{sj})\,(1 - x^2/a^2) + n_{sj} \quad , \tag{2}$$

$$T_j(x) = (T_{oj} - T_{sj})\,(1 - x^2/a^2) + T_{sj} \quad , \tag{3}$$

where R is the major radius, a smaller value for R would actually be more appropriate but we take this as a first approximation. a is the minor radius, and the suffix j stands for the particle species ($a = a_L = a_s$ in this case).

The Maxwell equation of the wave is written in the form as

$$\nabla \times \nabla \times \tilde{\vec{E}} + \frac{1}{c^2}\frac{d^2}{dt^2}\tilde{\vec{E}} = -\mu_o \frac{\partial}{\partial t}\left(\sum_j \tilde{J}_j + \tilde{J}_{ext}\right) \tag{4}$$

where $\vec{E}$ is the electric field of the wave, ω is the angular frequency and $\tilde{J}_j$ is the oscillating current carried by the j-th species of the plasma. The explicit form of the rf conductivity which is derived based on the kinetic

theory is shown in refs. [9,11] and is not repeated here. We take into account the finite gyro-radius effect up to the second order, the fundamental and second cyclotron resonances, the Landau damping as well as the transit time magnetic pumping. The boundary condition is given by

$$\frac{E_y'}{E_y} = \frac{E_z'}{E_z} = \mp \sqrt{k_z^2 - \frac{\omega^2}{c^2} - i\omega\mu_o\sigma_w} \quad \text{at } x = \pm b \qquad (5)$$

on the wall, where σ_w is the conductivity of the wall material. The antenna is simulated to be a current carrying ribbon, which has the arc length L_A, the toroidal width L_T and a zero thickness. The rf current on the antenna is in the y-direction and given as

$$\tilde{J}_A(\vec{r},t) = \sum_{k_z} J_A(k_z)\ \delta(x-d)\ e^{i(k_z z-\omega t)} \qquad (6)$$

(the sign -d corresponds to the low field side excitation).

In the following, we assume the current distribution on the antenna as $\tilde{J}_A(z) \alpha \exp(-4z^2/L_T^2)$. Because we take a linear approximation, Eq. (4) is solved by Fourier decomposition for each single k_z component. The two-dimensional structure on the equatorional plane is given by Fourier composition. The details of the numerical procedure are given in Ref. [11].

The power absorption to each species is given as

$$P_j(x,k_z) = \langle \tilde{J}_j(x,k_z)\ \tilde{E}(x,k_z) \rangle \qquad (7)$$

where the symbol $\langle\ \rangle$ indicates the phase average. Integrating in the x-direction, the power to j-th species through the k_z-Fourier component is given as $\bar{P}_j(k_z) = \int P_j(x,k_z)dx$.

The summation of $\bar{P}_j$ over j (j = i,e,w; w stands for the wall loss), $\bar{P} = \sum_j \bar{P}_j$, is the total damping of the k_z-th component. The total absorption is given as

$$\bar{P}_t = \sum_{k_z} \bar{P}(k_z) \qquad (8).$$

Similarly, total absorption to j-th species, $\bar{P}_{jt}$, is given as

$$\bar{P}_{jt} = \sum_{k_z} \bar{P}_j(k_z) \qquad (9).$$

The power deposition profile on the equatorial plane is given as (by firstly Fourier composing the field)

$$P_j(x,z) = < \tilde{J}_j(x,z)\, \tilde{E}(x,z) > \qquad (10).$$

The integral in the z-direction, $\hat{P}_j(x) = \int P_j(x,z)dz$, indicate the power deposition profile of the global wave excited by the antenna current, Eq.(6). The total absorption profile, $\hat{P}_t$, is defined as

$$\hat{P}_t(x) = \sum_j \hat{P}_j(x) \qquad (11).$$

The integral of $\hat{P}_t(x)$ in the x-direction agrees with $\bar{P}_t$. The loading impedance $\hat{Z} = \hat{R} - i\hat{X}$ is defined by

$$\tilde{E} = \tilde{Z}\ I_A \qquad (12)$$

on the antenna, and the loading resistance satisfies the relation

$$\overline{P}_t = \frac{1}{2} \hat{R} I_A^2 \qquad (13)$$

which corresponds to the energy conservation relation.

3) MINORITY HEATING

We first study the case of the minority heating. Geometrical and rf wave parameters are listed in Table I. The majority ions are deuterons and the minority ions are protons.

Fig. 3 shows a typical example of the wave form on the surface z = 0. The antenna is located on the low field side at z = 0 and x = d. The x-component and y-component of the electric field ((a), (b)) the power deposition profile $P_j(x)$ (c) are given for the parameters: $n_e(0) = 5 \times 10^{19}$ m^{-3}, $n_{es} = 10^{19}$ m^{-3}, T_o = 1 keV, T_s = 100 eV and n_H/n_e = 5 %. In the following I_A is chosen to be 1A unless otherwise specified. This graph shows that the fast wave penetrates into the core plasma, the mode-conversion takes place and that the minority ions absorb the wave energy over a wide range of the plasma column.

Humps and valey appear in $\hat{P}(x)$, because of the standing wave nature of the excited field. $\hat{P}(x)$ becomes small near the node of the wave field. The loading resistance and reactance are $\hat{R}$ = 1.4 Ω/m and $\hat{X}$ = 41.4 Ω/m. The ratio of the direct absorption is given as $\overline{P}_e$; $\overline{P}_D$; $\overline{P}_H$ = 4.5 %; 2.4 %; 93.1 %. Figure 3(d) shows the wave form in the toroidal direction on the x = d surface.

This plasma parameter simulates a target plasma which is generated by the ECH. In this density range, the perpendicular wave length of the fast wave is comparable to or longer than the typical scale of the plasma inhomogenity, a. It is therefore expected that the cavity resonance affects the antenna plasma coupling as well as the power depositon profile. The cavity resonance occurs for a k_Z-mode which satisfies the relation[9,21]

$$k_z^2 + \left(\frac{m\pi}{2a}\right)^2 = \frac{\omega^2}{\bar{v}_A^2} \qquad (14)$$

where m = 1,2, ... and $\bar{v}_A$ is the averaged Alfven velocity. To see this effect of the cavity resonance, we show in Fig. 4 the power absorption profile $\bar{P}(k_z)$ with the antenna current spectrum $|J(k_z)|^2$ for the density $n_{eo} = 2\times10^{19}m^{-3}$, $5\times10^{19}m^{-3}$ and $10^{20}m^{-3}$.

When the density is low, the perpendicular wave length becomes longer. The lowest order cavity resonance occurs at $k_zR = 5$ for the case $n_{eo} = 2\times10^{19}m^{-3}$. Figure 5 shows $\bar{P}$ for a particular value of k_z ($k_zR = 24$ for this case) as a function of density. n_s is kept constant. At the density of $n_{eo} = 1.9\times10^{19}m^{-3}$ a sharp resonance exists. A higher mode resonance, which is much broader, is observed near $n_{eo} = 5\times10^{19}m^{-3}$. Beyond the density $n_{eo} = 10^{20}m^{-3}$, a more stable coupling is expected.

Figure 6 shows the density dependence of the total loading resistance $\hat{R}$. Below the density $n_{eo} = 1.5\times10^{19}m^{-3}$ the accessibility is poor and the loading resistance is small. At the density $n_{eo} = 2\times10^{19}m^{-3}$, a strong peak in the loading resistance appears. This is because the low k_z modes satisfy the cavity condition Eq.(14). Because of the wide vacuum region between the plasma and the antenna, the accessibility of the large k_z mode is poor. In the large k_z limit, this vacuum region suppresses the power $\bar{P}(k_z)$ by the factor of $\exp[-k_z(d-a)]$. Above a central density of $n_{eo} = 10^{20}m^{-3}$, the loading is less affected by the cavity resonance. Figure 7 illustrates the wave form of the electric field in x-direction on the z = 0 plane with the power deposition profile, for the case of $n_{eo} = 10^{20}m^{-3}$. Partition of the absorption power is given as P_e; P_D; P_H; = 1.2 %; 3.8 %; 95 %.

From Figs. 3 and 7 it can be seen that the power deposition profile is peaked on a resonance surface, but has a wide half-width. The ions absorb the wave energy in the range $|\omega-\Omega_H| \lesssim 3\, k_z\, v_{TH}$ where Ω is the cyclotron frequency and v_{TH} is the thermal velocity of protons. Because the magnetic field varies as Eq.(1), this condition restricts the spatial region $|x-x_r| < \Delta_r$ for the absorption of the energy, where $\omega = \Omega_H(x_r)$ and

$$\Delta_r \simeq 3\ \rho_H\ k_Z\ R \qquad (15)$$

For the parameter of the analysis $\rho_H \simeq 0.12$ cm holds and Δ_r normalized to a is given as $\Delta_r/a \simeq 0.04\ k_Z R$. From the study of the wave coupling, the modes with $k_Z R < 30$ contributes to the power absorption. Taking $k_Z R \simeq 10\text{-}20$, we have an estimate

$$\frac{\Delta_r}{a} \simeq 0.4 - 0.8 \qquad (16)$$

The deposition profile becomes wide. For a wide range of parameters, the main absorption mechanism is the cyclotron resonance of minority ions.

4) SECOND HARMONIC CYCLOTRON RESONANCE HEATING

The second harmonic cyclotron resonance heating has the advantage that the wave length becomes shorter due to the higher frequency.

Figure 8 shows the k_z dependence of $\bar{P}$ for the 2nd harmonic cyclotron resonance of a pure hydrogen plasma. We choose $\omega/2\pi = 80$ MHz, $T_o = 2$ keV and $T_s = 0.1$ keV. Other parameters are the same as in Fig. 3. As in the case of minority ion heating, peaks which correspond to the cavity resonance appear for the low density case. If the density reaches to $2\times10^{20}m^{-3}$, the loading spectrum $\bar{P}(k_z)$ becomes a smooth curve. The difference of $\bar{P}(k_z)$ also results in the difference of the rf wave structure. Figure 9 shows the wave field $\tilde{E}_y(z)$ on the plane of the antenna, x=d. The field is strong near the antenna and becomes weak away from the antenna. In the case of high density, all the k_z modes contribute to the excited wave, so that the envelope of the wave is narrow. On the contrary, in the case of lower density, particlular components are strongly excited as a result of the cavity formation.

Figure 10 shows the density dependence of the loading resistance. Several peaks are observed in the lower density region. As the case for the minority heating, stable loading is possible in the higher density region of $n_{eo} > 10^{20}m^{-3}$. When the temperature is low, the damping is weaker and the density dependence of R becomes more peaked.

5) Generation of Fast Ions

The effects of the fast ions are of the particular interests for the nonaxisymmetric devices. In the collisionless regime, the high energy particles can be subject to a selective loss. This loss, on the other hand, can give rise to a radial electric field affecting the transport of bulk particles. We here briefly discuss the energy range of the high energy particle in the case of the minority heating.

Combining the wave propagation equation with the Fokker-Planck equation[9], the spatial distribution of the tail ion temperature has been obtained.[12,22-25] Applying the result to the present parameter, and assuming that the absorption profile is as broad as the average minor radius, we have an approximate estimate

$$T_h^{max}(\text{keV}) \simeq 5 \left(\frac{n_e}{n_H}\right) P_{rf}\ (\text{MW}) \qquad (17)$$

where T_h^{max} is the maximum temperature of the hot ion component. The central heating case with $\Delta_r \sim a$ is assumed and the plasma parameters are $n_{eo} \simeq 5\times10^{19}\text{m}^{-3}$ and $T_{eo} \simeq 2$ keV. In the case of $n_H/n_e = 5\%$, T_h^{max} can reach 40 keV at $P_{rf} \simeq 0.4$ MW.

The loss of fast ions with an energy of several 10 keV may be a serious problem. In the W VII-A experiment, the radial electric field was measured and analyzed[18]. The radial electric field is given by the balance of the fluxes of ions and electrons, Γ_i and Γ_e. If one assumes that the anomalous particle flux is ambipolar[26,27] and calculate Γ_i and Γ_e by the neoclassical theory for the bulk temperature, the equation $\Gamma_{e,th}^{nc} = \Gamma_{i,th}^{nc}$ gives the radial electric field[16,18]. (The suffix th stands for the contribution of the thermal particles). However, the analysis of the NBI injection (injection energy $E_b = 27$ keV) experiment has shown that the equation $\Gamma_{e,th}^{nc} = 10\ \Gamma_{i,th}^{nc}$ gives a better agreement with the experimentally observed electric field. (In the ECH case, on the contrary, the relation $\Gamma_{e,th}^{nc} = \Gamma_{i,th}^{nc}$ gives an approximate value of the radial electric field.)

Because the net ion flux must be equal to the electron flux, this fact implies the existence of an additional loss, the magnitude of which is more than $9\Gamma_i^{NC},_{th}$ of fast ions. There may be lots of other explanation of these phenomena, but one interpretation is that at the energy of the injection the loss of fast ions, Γ_i (non thermal), can reach 9 times of $\Gamma_i^{NC},_{th}$. If we assume that the same mechanism of the ion loss works in the ICRF heated plasmas as in the case of NBI, then at the power level of 0.3 MW, a similar phenomenon, i.e., the loss of fast particles and enhancement of the radial electric field, may be observed.

6) Summary and Discussion

By employing a simplified slab model of the plasma, we have studied the loading resistance and the wave form for the cases of the minority heating and the second harmonic cyclotron resonance heating.

The accessibility of the plasma is good for a density of $n_{eo} \geq 2\times10^{19}m^{-3}$. Above the density of $n_{eo} > 10^{20}m^{-3}$, a stable loading of $O(1\Omega)$ is expected. In an intermediate range of the density, the cavity mode affects the wave coupling. The loading resistance has sharp peaks as a function of density. This strong density dependence of R cast a problem for the high power injection. With a small change of the density, the loading resistance can change appreciably; the reflected power from the torus to the rf generator can vary quickly.

The cavity resonance has been predicted in the theoretical study[21]. In Heliotron-E device it was also predicted[20] and has later been confirmed by the experiment[7]. The cavity resonance is also expected to occur in the W VII-AS experiment. The half width of the cavity resonance should however be much wider than was calculated. The sharpness of the peaks obtained in this article is the upper bound, because we neglect the inhomogenity in the z-direction. Due to the inhomogeneity in the toroidal direction, the cavity effect would be smaller in the actual experiment.

We briefly discuss the energy level of the high energy ions. Extending the results of the W VII-A Stellarator, one may expect an important loss of fast ions in the range of $P_{rf} \sim 0.5$ MW.

We do not show the effect of the phase difference between two ICRF antennas. If one operates in the opposite-phase condition, then the small k_z components are reduced and the effect of the cavity resonance may be smaller. This operation scenario of the phasing also has worked for the reduction of the impurity in tokamaks[28,29].

It is also possible to calculate the optimum antenna dimensions for the given plasma parameter. This would be a straight forward extention of the present analysis. If the experiments with the present ICRF antenna prove that our understanding on ICRF wave in stellarators is correct, then an antenna design for given parameters can be obtained by performing the numerical simulation of this kind.

Table I

Magnetic field	B_o = 2.7 T	
Plasma Major Radius	R = 2 m	
Plasma Minor Radius	a = 0.09 m	
Vertical Minor Radius	a_v = 0.20 m	
Antenna Location	d = 0.16 m	(low field side)
Wall Minor Radius	b = 0.21 m	
Antenna width	L_T = 0.2 m	
Antenna Arc Length	L_A = 0.71 m	
Majority (Minority)ion	D(H)	
Ion Species for 2nd Cylotron Resonance Heating	H	
RF Frequency	40 MHz (Minority Heating)	
	80 MHz (Second Cyclotron Resonance)	

Acknowledgements

Autors wish to thank Mr. J. Kisslinger and Mrs. I. Ott for help in handling the computational code. Two of the authors (K.I. and S.I.I.) acknowledge the members of the W VII and ASDEX group and Dr. F. Wagner for hospitality during their stay at the Max-Planck-Institute für Plasmaphysik (IPP). Computations are performed by using the CRAY-1 in the computer center of IPP. Work partly supported by the Grant-in-Aid for Fusion Research of MoE Japan.

References

[1] Yoshikawa, S., Rothman, M.A. and Sinclair, R.M., Phys. Rev. Lett. 14 (1965) 214

[2] Equipe TFR, Plasma Phys. 24 (1982) 615.

[3] Hosea, J., et al., in Plasma Physics and Controlled Nucl. Fusion Research 1980 (IAEA, Vienna, 1981) Vol.2, 95.

[4] Mori, M., et al., in Plasma Physics and Controlled Nucl. Fusion Research 1984 (IAEA, Vienna, 1985) Vol.1, 445.

[5] Jacquinot, I., et al., Plasma Physics and Controlled Fusion 28 (1986) 1.

[6] Steinmetz, K., et al., Plasma Physics and Controlled Fusion 28 (1986) 235.

[7] Mutoh, T., et al., in Research Report PPLK-5 (Kyoto Univ.) 131

[8] Stix, T.H., Nucl. Fusion 15 (1975) 737.

[9] Fukuyama, A., Nishiyama, S., Itoh, S.-I., Itoh, K., Nucl. Fusion 23 (1983) 1005.

[10] Adam, , Plasma Physics and Controlled Fusion, 29 (1987) 443

[11] Fukuyama, A., Itoh, K., Itoh, S.-I., Computor Physics Reports 4 (1986) 137.

[12] Fukuyama, A., et al., in Proceedings of the 11th International Conference on Plasma Physics and Controlled Nuclear Fusion Research (Kyoto, 1986) paper F-IV-1.

[13] Noterdaeme, J.-M., et al, in Proceedings of the Topical Conference on the Application of RF Power to Plasma (Kissimnee, 1987), AIP Conference Proceedings 159, p. 242.

[14] Dorst, D., et al., Fusion Technology 1986 (Proceedings of the 14th Symposium, Avignon), Pergamon Press, 1986, Vol.1, 139.

[15] Hoffmann, D.J., et al., in Radio Frequency Plasma Heating (Madison, 1983) 224.

[16] Stringer, T.E., Phys. Fluids 13 (1970) 1586.

[17] Kovrizhnykh, L.M., Nucl. Fusion 24 (1984) 435.

[18] H. Renner and W7A group, p. 23 as in [7]

[19] Itoh, S.-I., et al., in Plasma Physics and Controlled Nuclear Fusion Research 1984 (IAEA, Vienna, 1985) Vol.1, 541.

[20] Fukuyama, A., Okazaki, N., Goto, A., Itoh, S.-I., Itoh, K., Nucl. Fusion 26 (1986) 151.

[21] Itoh, K., Itoh, S.-I., Fukuyama, A., Nucl. Fusion 24 (1984) 13.

[22] Morishita, T., Fukuyama, A., Hamamatsu, K., Itoh, S.-I., Itoh, K., Nucl. Fusion 27 (1987) in press.

[23] Itoh, S.-I., et al. "ICRF Heating Analysis on ASDEX Plasmas" (IPP Report 3/115, 1987).

[24] Itoh, S.-I., et al., in Proc. 14th European Conference on Controlled Fusion and Plasma Physics (Madrid, 1987) Vol. III 1204.

[25] Hamamatsu, K., et al., ibid. Vol.III 861.

[26] Inoue, S., et al., Nucl. Fusion 19 (1979) 1253.

[27] Horton, C.W., Plasma Physics 22 (1980) 345.

[28] Itoh, K., Fukuyama, A., Itoh, S.-I., Comments on Plasma Physics and Controlled Fusion 10 (1986) 91.

[29] Tamai,H., et al., Nucl. Fusion 26 (1986) 365

Figure Captions

Fig. 1 The geometry of the Wendelstein VII-AS stellarator in the vicinity of the ICRF antenna. The poloidal cross-section (a) and the cross-section on the equatorial plane (b). Numbers in the figure show dimensions in mm.

Fig. 2 The model geometry of the analysis. x-axis corresponds to the direction of the major radius, z-axis is taken in the toroidal direction, and the wall is located at x = + d. The plasma is assumed uniform in y- and z-direction.

Fig. 3 Typical wave form in the plasma for the case of minority heating. The x- and y-components of the electric field in the plane z=0 (a;b). The power depostion profile (c) and the electric field in the vacuum region $E_y(z)$ on the plane x=d (antenna position) (d) are also shown. Plasma parameters are $n_{eo} = 5\times10^{19}m^{-3}$, $n_{es} = 10^{19}m^{-3}$, $T_o = 1$ keV, $T_s = 0.1$ keV and $n_H/n_e = 0.05$.
$I_A = 1A$ and other parameters are in Table I. The power partition is $P_e : P_D : P_H = 0.045 : 0.024 : 0.93$ in this case.

Fig. 4 Absorption spectrum $\bar{P}(k_z)$ for the case of the minority heating case. n_{eo} is chosen to be $2\times10^{19}m^{-3}$, $5\times10^{19}m^{-3}$ and $10^{20}m^{-3}$.
In the low density case, cavity resonances are observed.

Fig. 5 Power absorption for particular k_z component as a function of $n_e(0)$. Solid line is for $k_zR = 12$ and dashed line is for $k_zR = 24$.
Sharp and high resonance is observed near the density of $n_e(0) = 2\times10^{19}m^{-1}$. In the higher density region, the higher mode cavity resonance exists, but the peak is broader.

Fig. 6 The loading resistance as a function of the plasma density. Below the density of $n_e(0) \sim 2\times10^{19}m^{-3}$, coupling is poor. The lowest order cavity resonance appears at $n_e(0) \sim 2\times10^{19}m^{-3}$. Above the density of $n_e(0) \sim 10^{20}m^{-3}$, a smooth dependence of $\hat{R}$ on n_e is observed. Other parameters are the same as in Fig. 3.

Fig. 7 The wave form in the high density case (minority heating). $n_e = 10^{20}m^{-3}$ and other parameters are the same as in Fig.3.

Fig. 8 Power absorption spectrum $\bar{P}(k_z)$ for the second cyclotron resonance heating of the pure hydrogen plasma. $n_e(0)$ is chosen to be $5\times10^{19}m^{-3}$, $10^{20}m^{-3}$, $1.5\times10^{20}m^{-3}$ and $2\times10^{20}m^{-3}$. T_o = 2 keV, T_s = 0.2 keV, $\omega/2\pi$ = 80 MHz, I_A = 1A and other parameters are in Table I.

Fig. 9 Comparison of the wave form in the vacuum region for high density (a) and low density (b) cases (second cyclotron resonance heating of hydrogen plasma). The form of $E_y(z)$ on the x=d plane is shown. When the damping is large (a:$n_{eo} = 2\times10^{20}m^{-3}$), the wave is localized near the antenna.

Fig. 10 The loading resistance of the antenna as a function of the density for the second cyclotron resonance heating.

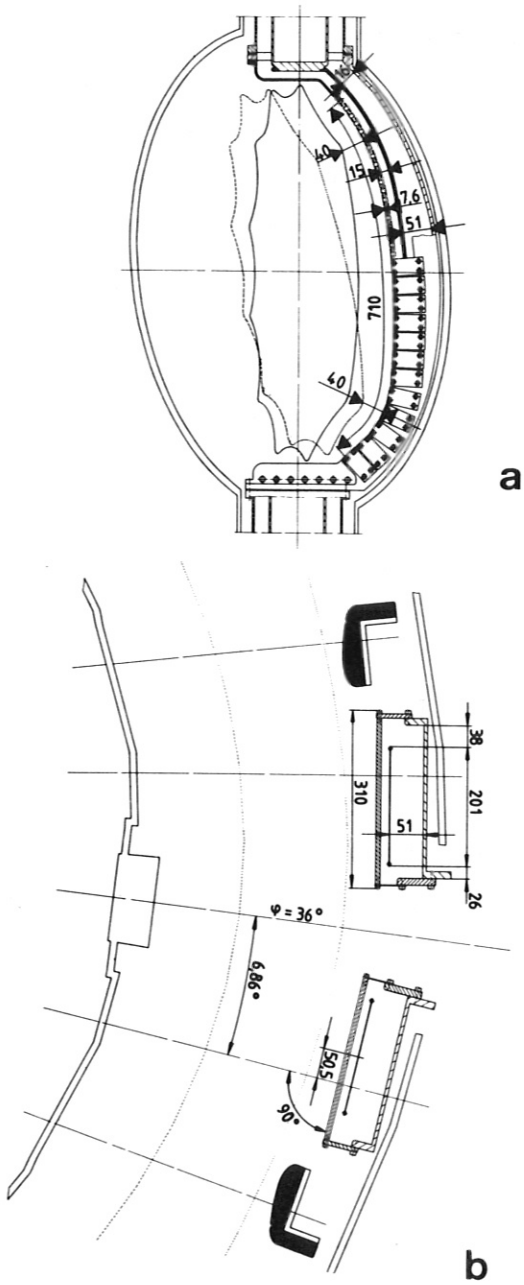

Fig. 1 The geometry of the Wendelstein VII-AS stellarator in the vicinity of the ICRF antenna. The poloidal cross-section (a) and the cross-section on the equatorial plane (b). Numbers in the figure show dimensions in mm.

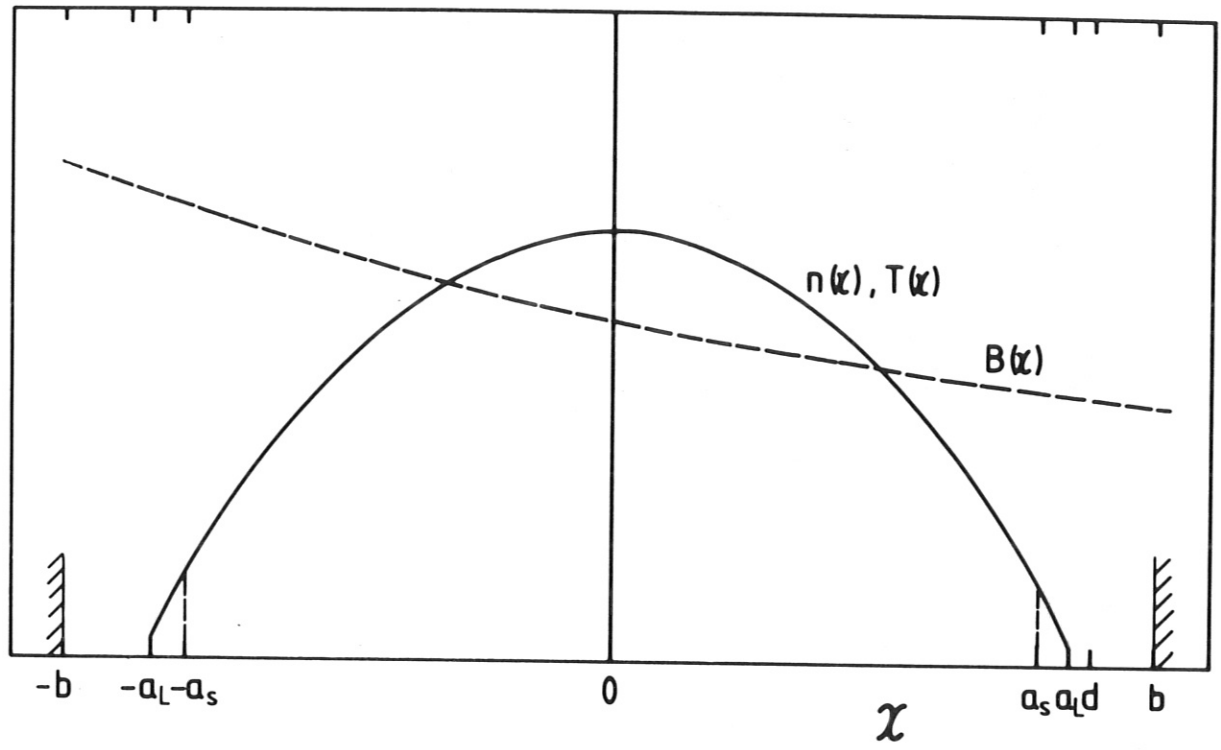

Fig. 2 The model geometry of the analysis. x-axis corresponds to the direction of the major radius, z-axis is taken in the toroidal direction, and the wall is located at x = + d. The plasma is assumed uniform in y- and z-direction.

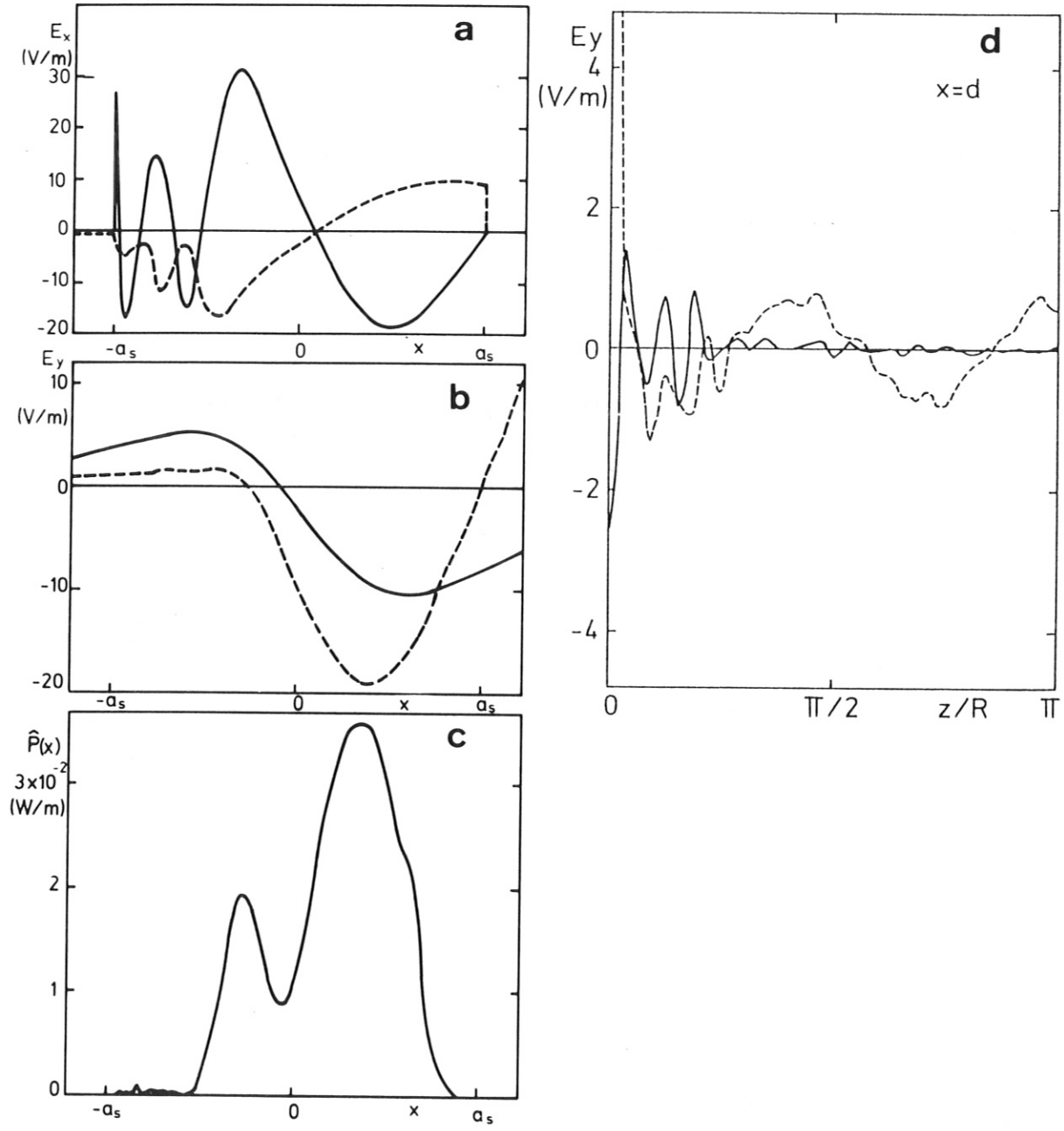

Fig. 3 Typical wave form in the plasma for the case of minority heating. The x- and y-components of the electric field in the plane z=0 (a;b). The power deposition profile(c) and the electric field in the vacuum region $E_y(z)$ on the plane x=d (antenna position) (d) are also shown. Plasma parameters are $n_{eo} = 5\times10^{19}m^{-3}$, $n_{es} = 10^{19}m^{-3}$, $T_o = 1$ keV, $T_s = 0.1$ keV and $n_H/n_e = 0.05$.
$I_A = 1A$ and other parameters are in Table I. The power partition is $P_e : P_D : P_H = 0.045 : 0.024 : 0.93$ in this case.

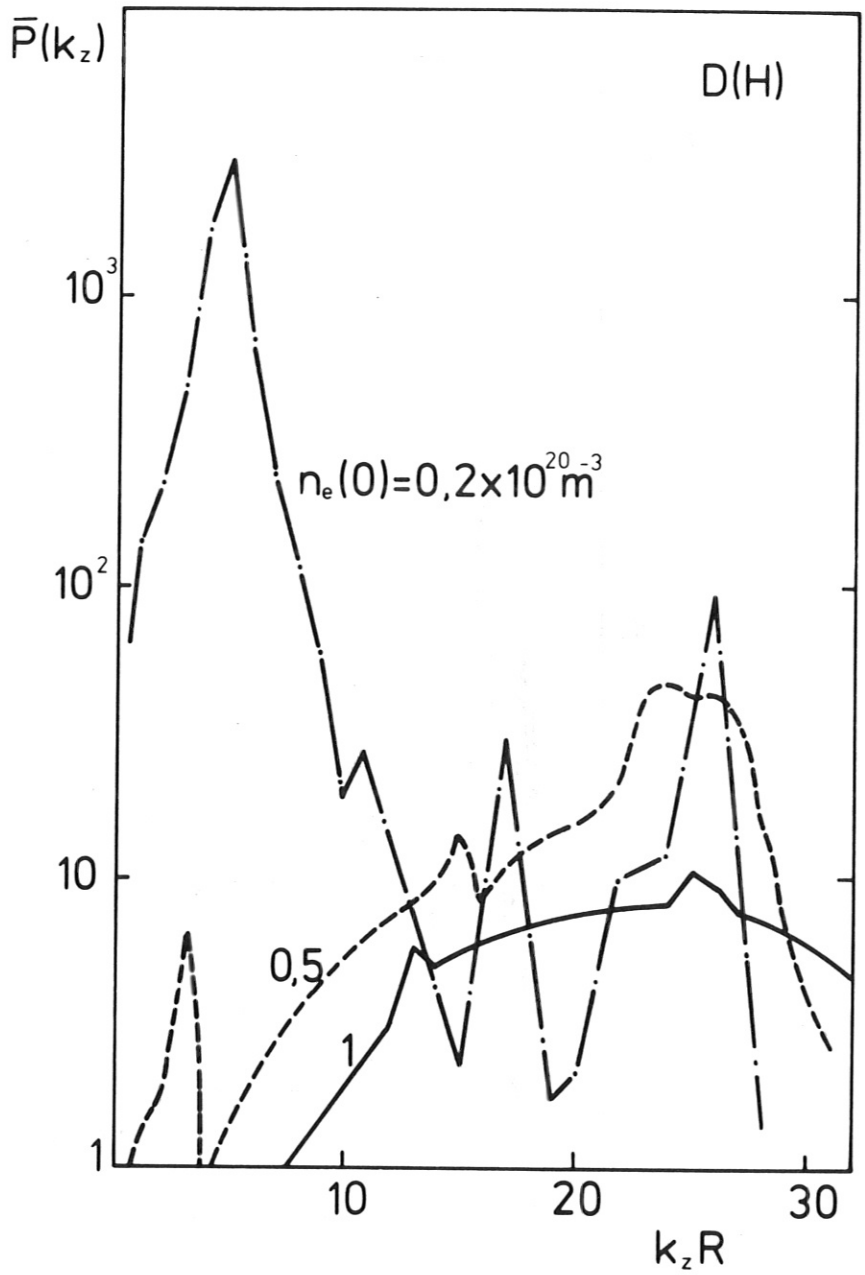

Fig. 4 Absorption spectrum $\bar{P}(k_z)$ for the case of the minority heating case. n_{eo} is chosen to be $2\times10^{19}m^{-3}$, $5\times10^{19}m^{-3}$ and $10^{20}m^{-3}$. In the low density case, cavity resonances are observed.

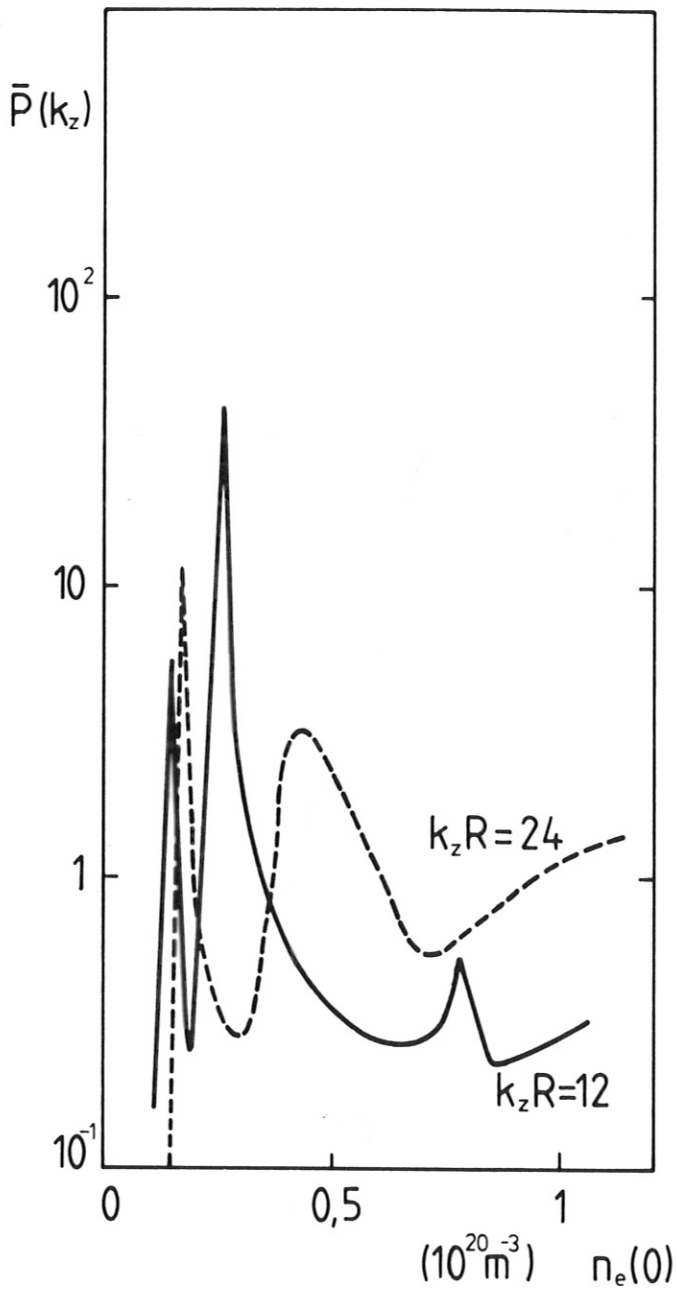

Fig. 5 Power absorption for particular k_z component as a function of $n_e(0)$. Solid line is for $k_zR = 12$ and dashed line is for $k_zR = 24$. Sharp and high resonance is observed near the density of $n_e(0) = 2x10^{19}m^{-1}$. In the higher density region, the higher mode cavity resonance exists, but the peak is broader.

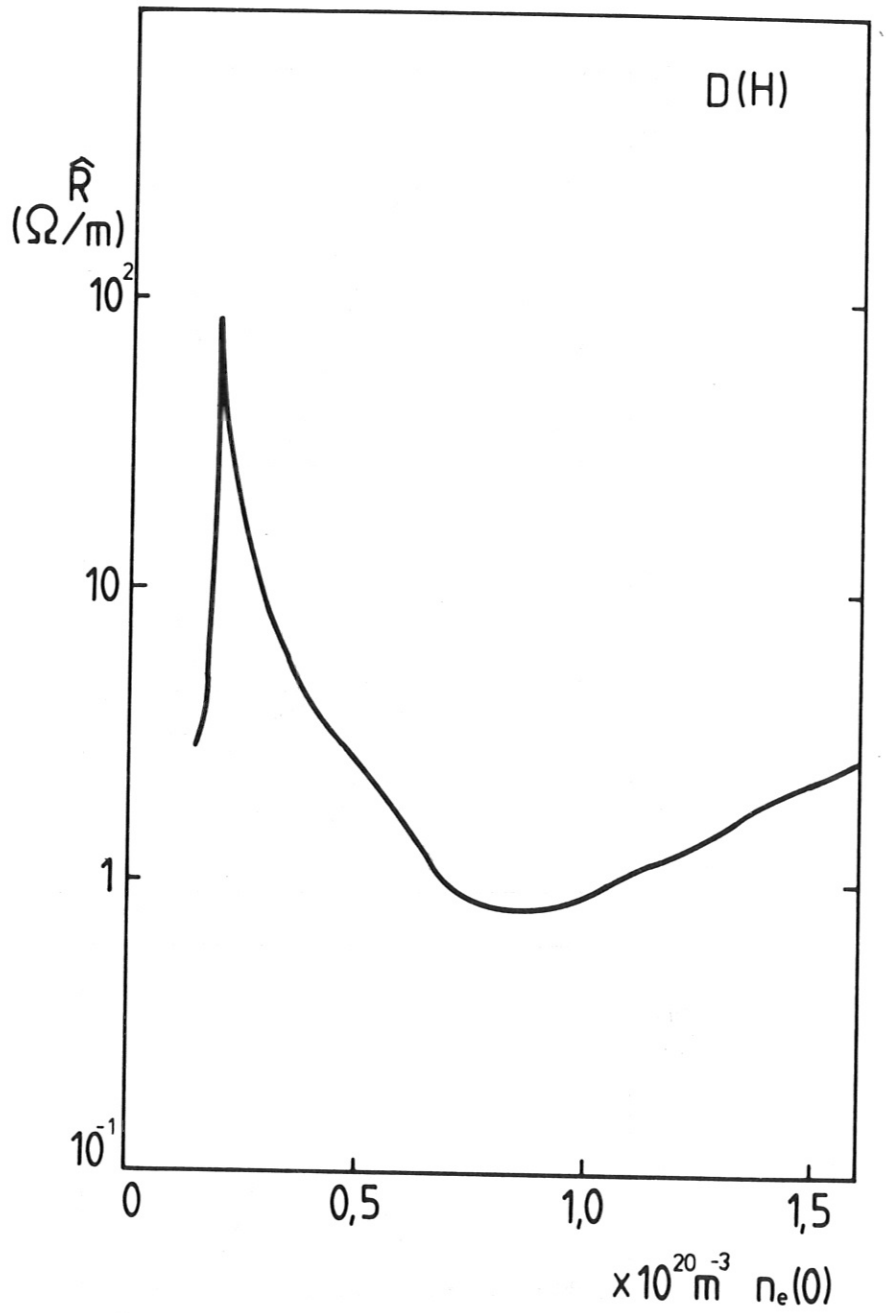

Fig. 6 The loading resistance as a function of the plasma density. Below the density of $n_e(0) \sim 2\times10^{19}m^{-3}$, coupling is poor. The lowest order cavity resonance appears at $n_e(0) \sim 2\times10^{19}m^{-3}$. Above the density of $n_e(0) \sim 10^{20}m^{-3}$, a smooth dependence of $\hat{R}$ on n_e is observed. Other parameters are the same as in Fig. 3.

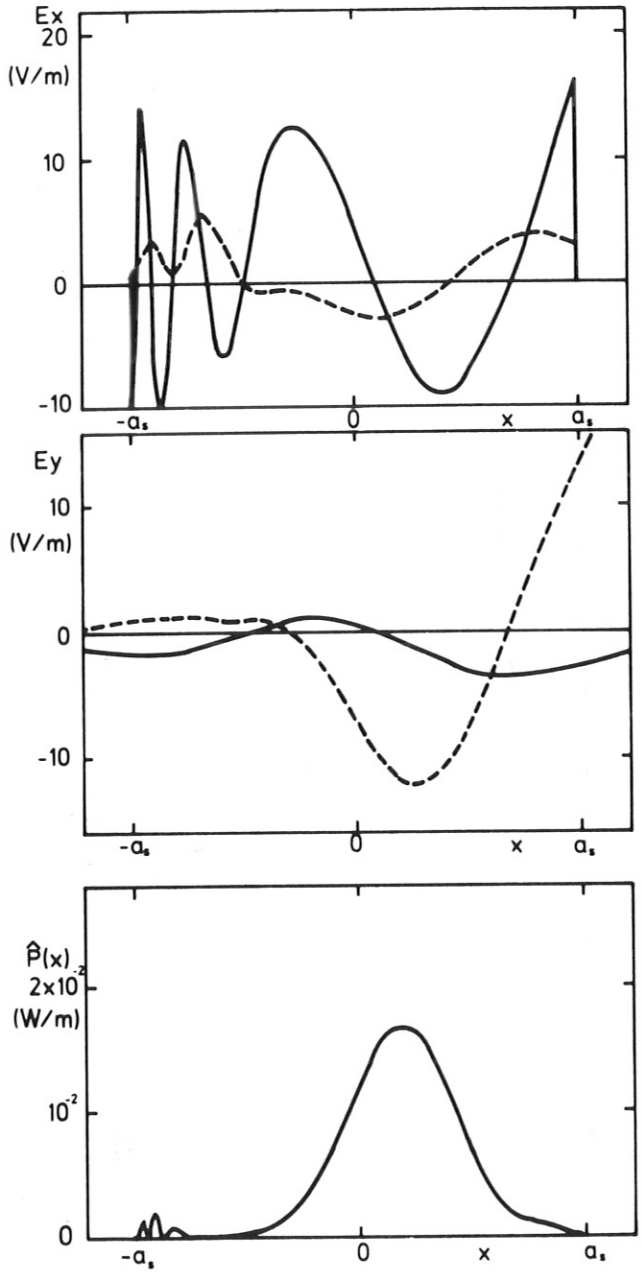

Fig. 7 The wave form in the high density case (minority heating). $n_e = 10^{20}m^{-3}$ and other parameters are the same as in Fig.3.

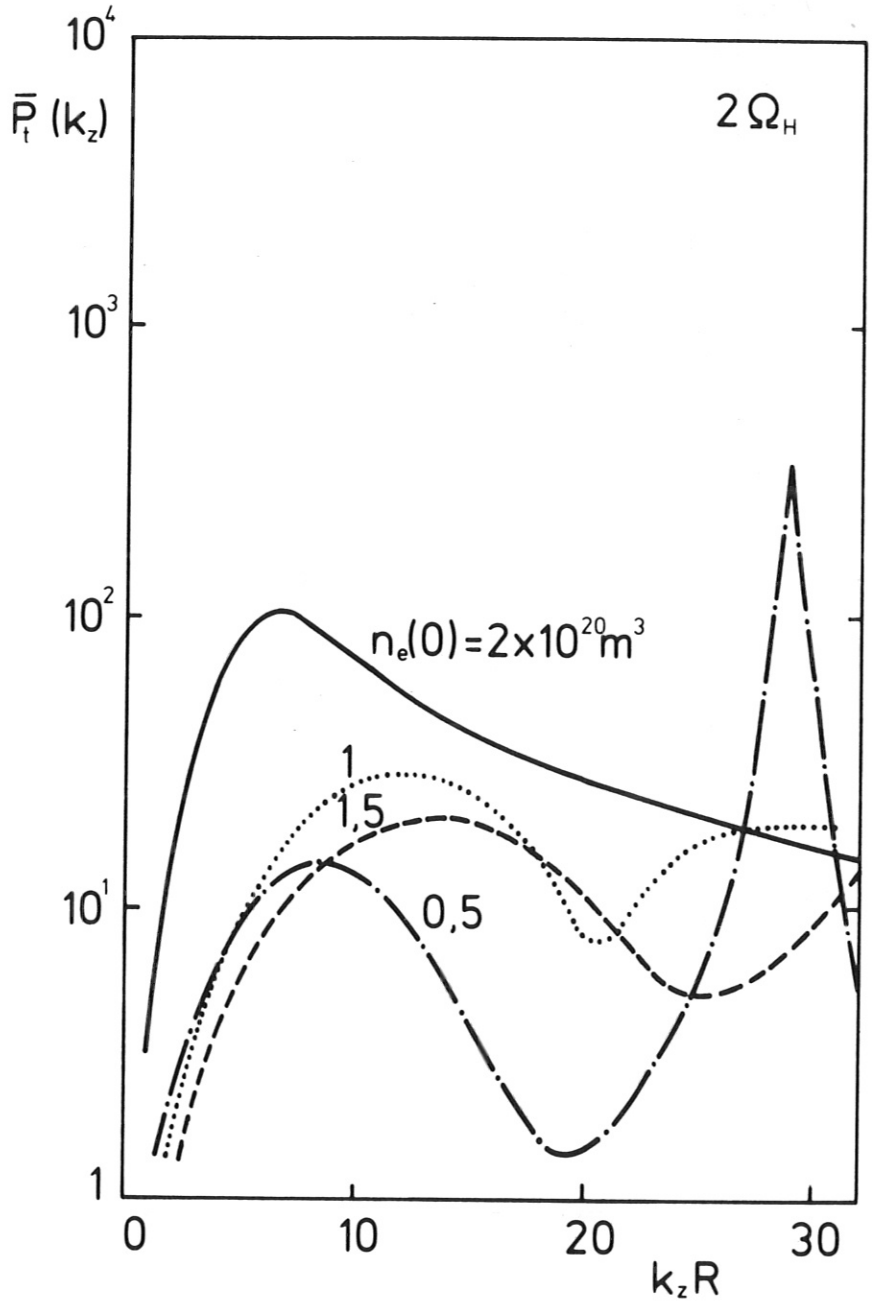

Fig. 8 Power absorption spectrum $\bar{P}(k_z)$ for the second cyclotron resonance heating of the pure hydrogen plasma. $n_e(0)$ is chosen to be $5\times10^{19}m^{-3}$, $10^{20}m^{-3}$, $1.5\times10^{20}m^{-3}$ and $2\times10^{20}m^{-3}$. T_O = 2 keV, T_S = 0.2 keV, $\omega/2\pi$ = 80 MHz, I_A = 1A and other parameters are in Table I.

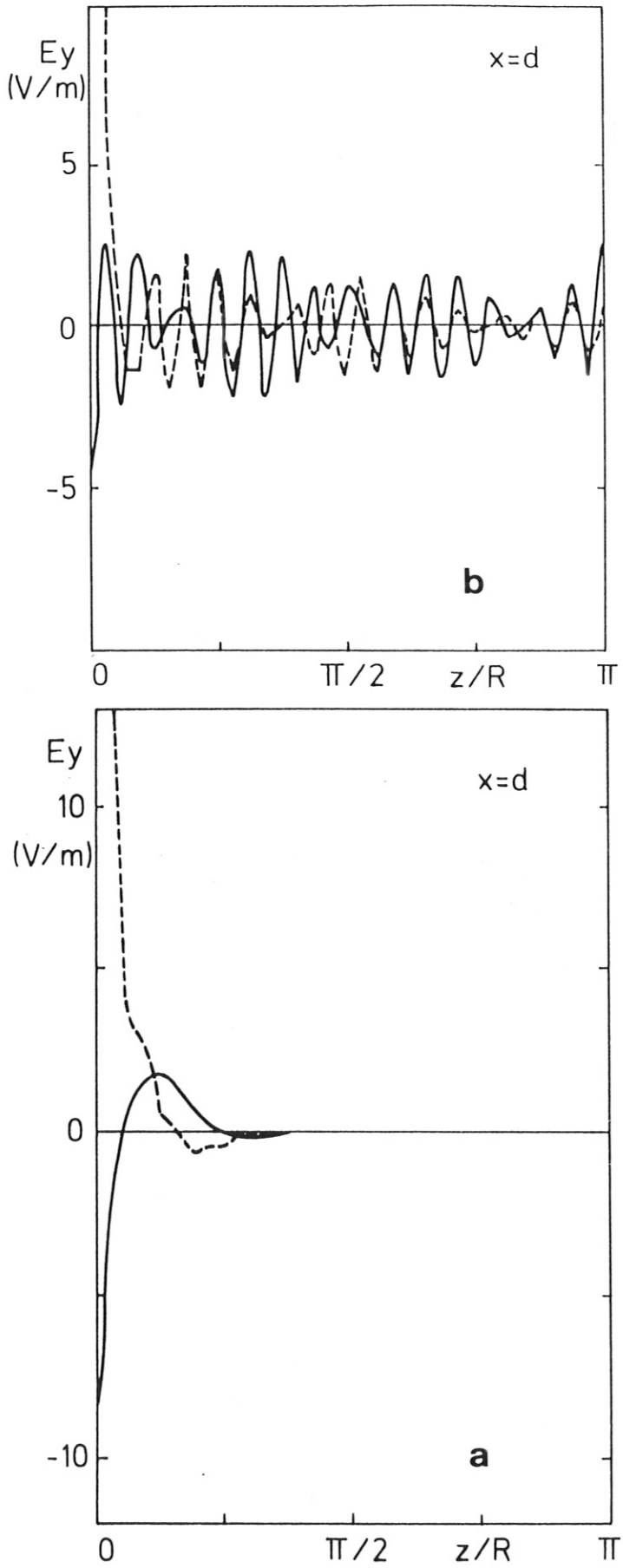

Fig. 9 Comparison of the wave form in the vacuum region for high density (a) and low density (b) cases (second cyclotron resonance heating of hydrogen plasma). The form of $E_y(z)$ on the x=d plane is shown. When the damping is large (a:n_{eo} = $2\times10^{20}m^{-3}$), the wave is localized near the antenna.

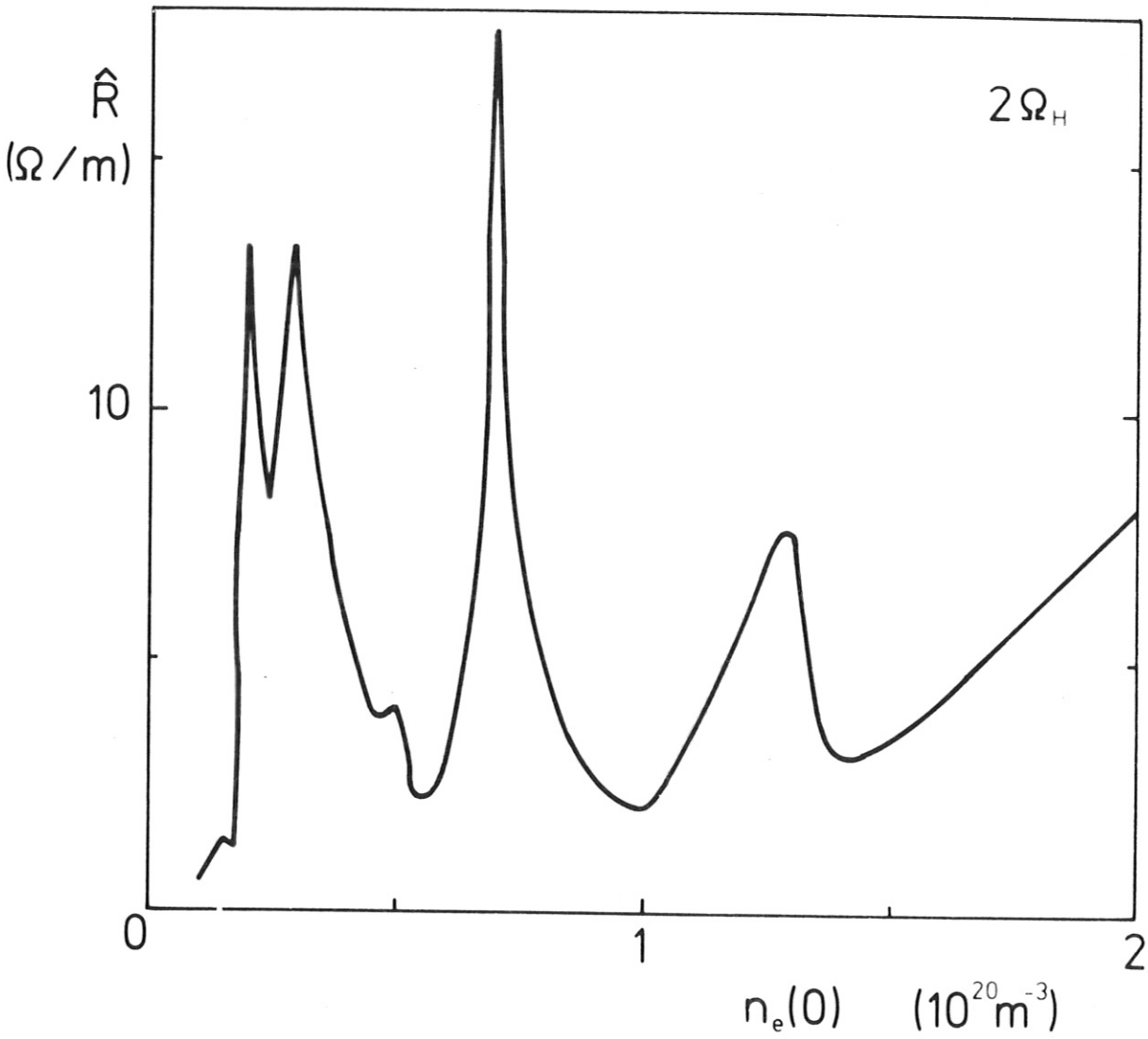

Fig. 10 The loading resistance of the antenna as a function of the density for the second cyclotron resonance heating.